Impact of soot deposits on waste gas-to-electricity conversion in a TiO_2/WO_3-based photofuel cell

Impact of Soot Deposits on Waste Gas-to-Electricity Conversion in a TiO_2/WO_3-based Photofuel Cell

Karthick Raj AG[a,c], Antony Charles Minja[a,c], Rajeshreddy Ninakanti[a,b,c], Myrthe Van Hal[a,c], Fons Dingenen[a,c], Rituraj Borah[a,c], and Sammy W. Verbruggen[a,c]*

[a] Sustainable Energy, Air & Water Technology (DuEL), Department of Bioscience Engineering, University of Antwerp, Groenenborgerlaan 171, 2020 Antwerp, Belgium

[b] Electron microscopy for Materials Science (EMAT), Department of Physics, University of Antwerp, Groenenborgerlaan 171, 2020 Antwerp, Belgium

[c] NANOlab Center of Excellence, Groenenborgerlaan 171, 2020 Antwerp, Belgium

Email: Sammy.Verbruggen@uantwerpen.be

Abstract

An unbiased photo-fuel cell (PFC) is a device that integrates the functions of a photoanode and a cathode to achieve simultaneous light-driven oxidation and dark reduction reactions. As such, it generates electricity while degrading pollutants like volatile organic compounds (VOCs). The photoanode is excited by light to generate electron-hole pairs, which give rise to a photocurrent, and are utilized to oxidise organic pollutants simultaneously. Here we have systematically studied various TiO_2/WO_3 photoanodes towards their photocatalytic soot degradation performance, PFC performance in the presence of VOCs, and the combination of both. The latter thus mimics an urban environment where VOCs and soot are present simultaneously. The formation of a type-II heterojunction after the addition of a thin TiO_2 top layer over a dense WO_3 bottom layer, improved both soot oxidation efficiency as well as photocurrent generation, thus paving the way towards low-cost PFC technology for energy recovery from real polluted air.

Keywords

Photofuel cell, Soot degradation, Air purification, Photoelectrocatalysis, TiO_2, WO_3,

1. Introduction

Energy conversion *via* combining the advantages of photocatalysis and electrocatalysis—photoelectrocatalysis (PEC), becomes a promising and capable alternative technology that neutralizes

toxic or harmful substances through redox reactions and produces green and sustainable energy carriers (fuels and electricity)[1–3]. PEC uses sunlight to oxidize volatile organic compounds (VOCs) at the photoanode and simultaneously recover part of the energy of these degraded compounds at the cathode as fuel or energy. The performance of PEC cells is influenced by several internal factors, such as the choice of catalyst, electrolyte pH, and stability. External factors such as temperature, humidity, incident light intensity, and accumulation of solid deposits on the electrodes, especially when a gas-phase cell is used outdoors, can hinder the active catalytic site and light absorption, ultimately reducing overall performance.

The highly polluted environment and higher soot accumulations both indoors and outdoors are global issues, particularly in urban and industrialized areas [4,5]. Soot, a particulate carbon matter, mainly originates from emissions and incomplete combustion of hydrocarbons from industries and vehicles[6]. Numerous studies have reported daily soot accumulation at different places with varying climatic conditions, ranging on average from several micrograms to a few hundred micrograms per square meter per day[7–10], depending on the ambient conditions. Therefore, in this present study, for the first time, we studied and mimicked the operation of an all-gas-phase photofuel cell (PFC) in a highly polluted environment using the model compound Printex-U with an average particle size of 25 nm and a surface area of 92 m^2/g. The addition or presence of soot hinders the light interaction as it covers the photoanode's active surface. It could also react with holes and other reactive oxidants at the photoanode. This could affect the overall PEC cell's performance. Therefore, the ability of a photoanode of a PEC cell to cope with soot deposits is crucial for obtaining stable and long-term operation in soot-contaminated (*i.e.*, urban) environments.

As a photoanode material, titanium dioxide (TiO_2) is a well-known benchmark photocatalyst with good chemical stability and high photo-reactivity [11]. Under UV illumination, TiO_2 is exceptionally active and degrades various organic and toxic pollutants, including dyes, soot, and volatile organic compounds[12,13]. The photocatalytic degradation of soot using TiO_2 has been extensively studied [14–21] and it is a convenient and less expensive technique compared to traditional high-temperature soot

destruction. Photocatalytic soot degradation was first reported by Lee *et al*. [17] in 2002, who studied the degradation at solid/solid interfaces facilitated by the migration of generated OH* radicals and achieved complete degradation in 30 hours. Later, it was confirmed by Mills *et al*.[16] who also studied the CO_2 mineralization of soot using FTIR (Fourier transform infrared spectroscopy) in consecutive work [15]. Smits *et al*.[19] studied the self-cleaning effect of mortar coated with TiO_2 and achieved 60% CO_2 mineralization in 24 hours, and Kameya *et al*. [14] investigated the influence of porous and microstructured TiO_2 nanoparticles on soot degradation. Van Hal *et al*. [20,21] extensively studied different photocatalysts for soot degradation and used an improved digital image analysis technique along with an *in situ* FTIR technique to monitor and study the reaction pathway.

In recent times, photoanodes made up of tungsten trioxide (WO_3) have attracted more attention due to their good photochemical stability and high visible light absorption [22]. Specifically, in the dark, the oxygen evolution at WO_3 electrodes takes place at >2 V *versus* the normal hydrogen electrode (NHE) at pH 0, which means it has an overpotential of >0.8 V, whereas under the illumination of air mass (AM) 1.5G, the oxygen evolution occurs at 0.6 V versus NHE with a shift of 1.4 V [23–25], making it a highly suitable photoanode material. The concept of an all-solid-state PEC was proposed by Seger *et al*. [26] in 2009 using a TiO_2 photoanode and Pt cathode with no applied bias. Georgieva *et al.* [27] showed photo-oxidation of 10% w/w methanol vapours using a TiO_2/WO_3 coated steel mesh photoanode and a platinum cathode at an applied bias of 0.5 V *vs* Ag/AgCl , yielding a photocurrent below 20 $\mu A/cm^2$. Other consecutive studies using composites of TiO_2 followed a similar trend [28,29]. Based on earlier research[30] that achieved state-of-the-art photocurrent generation of ~150 $\mu A/cm^2$ from WO_3 photoanodes in the abatement of model VOCs under aerobic conditions by an unbiased PFC cell, the idea was expanded to encompass tolerance towards soot deposits, while taking advantage of a broader light absorption range by embedding TiO_2 on WO_3. Combining and forming heterostructures of TiO_2 and WO_3 is expected to increase the solar utilization efficiency by covering both the ultraviolet (UV) and a part of the visible (VIS) light ranges. In addition, appropriate conduction band energy alignment allows for easy electron transfer between the conduction bands of WO_3 and TiO_2, ultimately improving charge transfer and separation efficiency [31–33].

In this study, the most promising TiO_2 and WO_3-based photocatalysts from earlier studies were selected based on their soot oxidation capacity and photoanode performance [21,30]. The selected photocatalysts were combined to form heterostructures by both mixing and layering strategies, and subsequently, the performance of the obtained photocatalyst combinations, both as soot degraders and photoanodes, was studied in the presence of VOCs as hole scavengers. Finally, a layer of soot was deposited on the best-performing catalyst combination. An image-based soot oxidation detection methodology was applied to simultaneously monitor the soot degradation efficiency as well as the effect of soot on the PFC operation. In addition, to better understand the generation of intermediates and CO_2 for the best-performing catalyst, an *in-situ* FTIR method was applied. As a final demonstration, the in-house-engineered PFC device was applied outdoors, serving as a proof of concept for a PFC system operating autonomously, solely using sunlight and outdoor air to generate sustainable electricity.

2. Experimental Section

2.1. Material Synthesis and Characterisation

The combination of TiO_2 and WO_3-based photocatalysts was studied and prepared using commercially available Aeroxide® P25 with anatase, rutile and an amorphous fraction in a ratio of 78:14:8, and a surface area of 35-65 m^2 g^{-1} from Evonik [34,35], and tungsten trioxide (WO_3) synthesized according to Martínez-de la Cruz *et al.* [36]. In brief, a precipitation method was used whereby 0.01 M of ammonium tungstate hydrate (99.9%, Aldrich) was dissolved in 67 ml of deionized (DI) water at 80°C and the pH of the solution was adjusted from 5.95 to almost near zero (pH 0 – 0.15) by adding 45 ml nitric acid (65%, Chem Lab) dropwise. The solution was then kept at 80°C for 70 minutes under constant stirring. After that, the formed precipitate was allowed to settle down overnight and washed three times by centrifugation with DI water. Finally, the precipitates were dried at 80°C and calcined at 600°C for 3 hours, and the prepared samples were denoted as $WO_{3\ Mart.}$

Photocatalyst combinations were prepared by mixing and layering two pure photocatalysts in different mass and molar ratios. While P25-$WO_{3\ Mart.,\ mass}$ was obtained by mixing equal masses of both photocatalysts, P25-$WO_{3\ Mart.,\ mol}$ was generated by mixing both photocatalysts in an equal molar ratio. A second combination strategy was to combine both photocatalysts in a layered configuration. After

drop-casting an appropriate amount of photocatalyst and drying it overnight at 85 °C forming the first photocatalyst layer, the second layer was drop-casted on top of the first layer, again followed by overnight drying at 85 °C. Different amounts of photocatalyst were applied, starting from a previously optimized standard total loading of 1.6 mg cm^{-2}. The photocatalyst combination is denoted by the photocatalyst loading of each material involved, from top to bottom, expressed in mg cm^{-2}. For example, the photocatalyst combination denoted as 'P25 on $WO_{3\ Mart.}$ (0.8/0.8)' is obtained by adding a layer of 0.8 mg cm^{-2} P25 on top of a layer of 0.8 mg cm^{-2} $WO_{3\ Mart.}$.

A range of physicochemical characterisation techniques (N_2 sorption, UV-VIS spectroscopy, and X-ray diffraction) was performed to characterise both pure and mixed photocatalysts. UV-VIS diffuse reflectance spectroscopy (DRS) was performed using a Shimadzu UV-2600 spectrophotometer, and Tauc's plot method was used to determine the band gap (E_g) of each photocatalyst. Micromeritics Tristar 3000 surface area and pore size analyser was used to perform N_2 adsorption/desorption measurements at -196 °C (liquid nitrogen). Before the measurements, the samples were degassed at 200 °C for 24 hours under a nitrogen atmosphere. X-ray diffraction (XRD) measurements were performed to determine the crystalline structure of the synthesized photocatalysts using a Bruker D8 Advance diffractometer with Cu K_α radiation of 1.54 Å, 40 kV, 40 mA and from 20-80 degrees with the applied scan rate of 0.5 s $step^{-1}$. Scanning electron microscopy (SEM) images were acquired to study surface morphology characteristics using FEG-ESEM-EDX, Thermo Fisher Scientific Quanta 250 at an accelerating voltage of 20 kV.

2.2. Photo Fuel Cell Measurements

The photofuel cell design and the preparation of the membrane electrode assembly (MEA) were described in detail in our previous work [30]. In brief, for a standard MEA, the photoanode consists of 1.6 mg cm^{-2} of photocatalyst mixed with 5 wt% Nafion® in isopropyl alcohol (IPA) (Fuel Cell Earth) and drop-casted on Toray carbon paper 030 (Fuel Cell Earth). The cathode consisted of 0.4 mg cm^{-2} platinum nanoparticles on carbon black (Sigma-Aldrich) mixed with 5wt% Nafion® in IPA and drop-

casted on Toray carbon paper 030. Both electrodes were dried overnight at 80 °C and a MEA was obtained by hot-pressing both the photoanode and cathode on opposite sides of a preconditioned Nafion® 117 membrane (Fuel Cell Earth) after the addition of 12 µL of a 5 wt.% Nafion® solution on the anode side. The hot-pressing conditions were 5.5 tonnes at 135°C for 3 minutes. The residual solvent was removed by exposing the MEA to UV-A illumination (320-400 nm) in a humid atmosphere overnight.

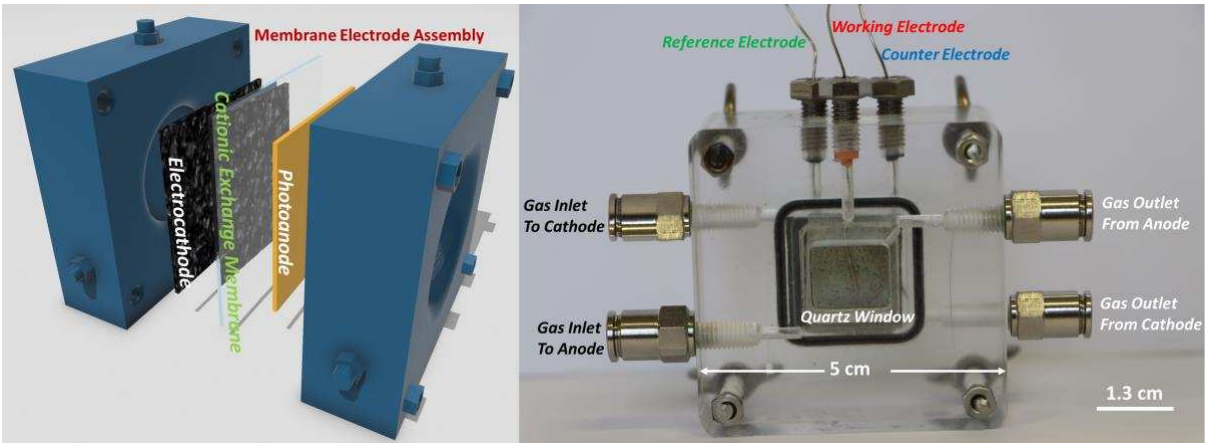

Figure 1. Cross-sectional view of the membrane electrode assembly (MEA) and its components positions (on the left); Front view of a three-electrode photo fuel cell (right).

Figure 1 (right) shows, the homemade PFC with the dimensions of 50 mm length (L), 50 mm height (H) and 30 mm width (W) comprising two compartments made up of chemically resistant poly (methyl methacrylate) (PMMA), engraved with a quartz window (13 mm (L) and 13 mm (H)) added to the anode compartment to obtain UV transparency. Six in- and outlet channels with an internal diameter of 1.2, 1, 0.8, 0.8, 1, and 1.2 mm from top to bottom, were added to the anode compartment to obtain a homogeneous flow pattern throughout the compartment. Stainless steel wires were used to connect the anode and cathode and as a *pseudo*-reference in the three-electrode configuration. The prepared MEAs were placed in the centre of the PFC device, between the anode and cathode current collectors in the compartment. For the UV light measurements, a Philips fluorescence S 25 W UV-A lamp was placed 3 cm from the photoanode surface, reaching an incident intensity of 2.35 mW cm^{-2} (between 290 and 400 nm, λ_{max} at 354 nm), as measured with an Avantes Avaspec-3648-USB2 spectroradiometer. The

simulated solar light measurements were performed using a 300 W Xe source (Oriel Instruments), equipped with an AM 1.5G filter to provide simulated solar light adjusted to a total irradiance of 100 mW cm^{-2} (between 300 and 1100 nm). For visible light measurements, a 420 nm cut-on filter was added. The absolute irradiance spectra for all used lamps are presented in **Figure S1** of the supplementary information.

All-gas-phase experiments were performed using a fully automated gas test setup developed in our group [37]. Water and methanol vapours were introduced into the gas flow by a gas wash bottle, and synthetic air (Messer) was bubbled through the bottle at a flow rate of 50 ml min^{-1}. The gas wash bottle was filled with either pure deionized water, obtaining moist air, or a 3 wt.% methanol aqueous solution, resulting in a moist vapour with a methanol concentration of 17 mmol m^{-3} (2573 ppmv). To achieve stable photocurrent generation, the photoanode compartment of the PFC was flushed with vapour for 30 minutes before each measurement. The cathode was not flushed but kept exposed to air. A VersaSTAT3 potentiostat (Princeton Applied Research) was used for all chronoamperometric (CA) and other electrochemical measurements.

2.2.1. *Electrochemical Measurements*

The photoelectrochemical response of pure catalyst as photoanode was investigated in a three-electrode configuration using an aqueous 0.5 M Na_2SO_4 (pH 7) electrolyte with Ag/AgCl (3.5 M KCl) reference electrode and a platinum counter electrode. The individual performances of pristine TiO_2 and $WO_{3\ Mart.}$ electrodes were evaluated using linear sweep voltammetry (LSV), chronoamperometry (CA), and electrochemical impedance spectroscopy (EIS) techniques to study the electrode/electrolyte interfaces, stability, and charge transfer rates. Mott Schottky analysis was performed using the protocol consistent with Gelderman *et al.* [38] to study the flat band potential of both pristine TiO_2 and $WO_{3\ Mart.}$ A detailed explanation of the electrochemical performance of each pure photocatalyst is given in the supplementary information along with **Figures S2,3,15,18.**

2.3. Photocatalytic Soot Oxidation

A detailed description of the coating and image analysis procedures can be found in our previous work [21]. In short, the photocatalysts were deposited on cleaned glass slides with a standard loading of

1.6 mg cm^{-2} by drop-casting. The coated glass slides were dried to remove residual solvent. Soot (Printex-U, Evonik) was deposited on top of the photocatalyst layer with a loading of 22 µg cm^{-2}, and the glass slides were again dried to remove all residual solvent shown in **Figure S4**. The photocatalyst combination of P25 on $WO_{3\ Mart.}$ (1.6/1.6) was excluded from the experiments due to large cracks in the P25 layer (**Figure S4(a)**).

The colour-based image analysis method used in our previous work [20,26] was used to monitor the soot degradation. The prepared samples were placed 3 cm away from a Philips fluorescence S 25 W UV-A lamp with an incident light intensity of 2.1 mW cm^{-2} in the region of 290-400 nm (λ_{max} at 354 nm). To ensure repeatability, the pictures were taken in a standard photobox fixed with a Canon EOS 500D in manual mode (ISO 200, aperture F8, and focal exposure 1:5) at a maximal resolution of 5184 × 3456 at 72 dpi. The image processing was done by using Image J freeware in standard CIELab colour space with perceptual lightness (L*) coordinates, which are used to measure the soot deposition amount on the photocatalytic surface with a brightness axis ranging between 0 (black) and +100 (white). Instead of predefining a pixel with threshold values as either fouled with soot or completely clean, the change in the L* coordinates in most of the pixels is taken as the measure for soot degradation. It is an easy approach to physically visualize and observe the soot degradation when the pixels become brighter, resulting in a higher shift of most of the frequent L* values, *i.e.*, +100, white. This results in a more realistic representation of the soot degradation and cleaning of the surface.

Each photocatalyst was applied onto five glass slides, and soot was deposited on four of them (*i.e.*, standard samples). Three standard samples were illuminated, and one was kept in the dark as a negative control. The glass slides containing only photocatalysts were illuminated together with the standard samples (*i.e.*, light-control samples). Digital images were taken from the glass slides before and after soot deposition at specific UV illumination intervals (0, 5, 11, 20, 26, 40, 61, and 82 days). In the VIS and daylight experiment, pictures were taken before soot deposition and after 0, 5, and 11 days of illumination. The comparison between the different photocatalyst combinations was made based on the shift in the most frequent L* value expressed relative to the most frequent L* value of the completely fouled sample. The probable deviation caused by the minor changes in the background was corrected

by processing a set area of the background and applying the L* deviation values to the complete dataset for that specific time.

To get an understanding of the photocatalytic activity at the catalyst surface, an *in-situ* FTIR analysis was performed using the patented cell design by Hauchecorne et al[39]. Extensive information on the cell design and reaction conditions can be retrieved from Van Hal *et al*, and Hauchecorne *et al*[21,39]. The sample made in the form of a pellet consisting of 5 mg of photocatalyst with 0.6 wt% soot (Printex-U) was properly mixed with 115 mg of potassium bromide (KBr) and pressed at 8 tons for 2 mins. Then the prepared sample was placed at the centre of the *in situ* cell and the reactor was flushed with synthetic air at the rate of 200 ml/min until a stable readout was obtained. Then the reactor was sealed airtight and illuminated with eight UV LEDs at each side of the cell with an incident intensity of 330 μW cm^{-2} (350-420 nm, with λ_{max} at 377 nm). The reaction was carried out for 12 h to study the reaction and product formation at the interface.

2.4.Combined PFC and Soot Experiments

The complete soot oxidation capability of PFC systems was studied using the prepared MEAs to imitate the PFC operation in a highly polluted environment. For the soot deposition on MEAs, 40 μL of Printex-U suspension in methanol was ultrasonically treated for 1 hour and drop-casted on the active surface of the photoanode, thus obtaining a uniform coverage of 22 μg cm^{-2} of soot on the photoanode. The presence of volatile residues on the surface, such as methanol, was removed by heating the MEA in a vacuum oven at 50 °C for 2 hours without affecting the membrane or electrode materials.

A Philips fluorescence S 25 W UV-A lamp was placed 3 cm from the photoanode, reaching an incident intensity of 2.35 mW cm^{-2} (between 290 and 400 nm, wavelength of maximal intensity (λ_{max}) at 354 nm). The soot detection method is applied to monitor the degradation of soot during PFC operation. No concentrated soot spots were observed when depositing soot on the photoanode of a MEA. Hence, only the degradation of a uniform soot haze was determined. Photographs were taken from the photoanode side of the MEA before and after soot deposition at specific UV illumination intervals (0, 1, 3, 7, 10, and 14 days). Possible changes in background illumination were cancelled by processing a

set area of the background analogue to the pictures of the MEA and correcting for the obtained deviation in the maximal L* value. Long CA measurements were taken to investigate the photocurrent performance under illumination and continuous vapour flushing of the anode.

2.5.Cyclic Test and Product Monitoring

After initial activity screening, the best-performing MEAs with and without soot were subjected to a long cyclic test to evaluate their stability under both light and dark conditions, with moist methanol vapour flushing at the rate of 50 ml/min. The evolved products were analysed using an in-line gas chromatograph (GC) (Trace 1300, Thermo Scientific, equipped with FID detector using methanizer and Hayesep® 60-80^{o}, Mol sieve 5 A^{o} Columns) attached inline to the reactor outlet stream.

2.6. Outdoor Applications

The in-house engineered PFC device is tested for a real-life application aiming for autonomous PFC operation utilizing sunlight and outdoor air to generate sustainable electricity, and in the meantime, it also degrades the VOCs present in the atmosphere. The measurements were carried out in different places in Antwerp (a busy highway, a rooftop, and a university campus). The best-performing P25 on $WO_{3\ Mart.}$ (0.4/1.6) combination, pristine P25 and $WO_{3\ Mart.}$ were tested as photoanode materials. The energy generation was monitored by using an ammeter (Kopp, Pan multimeter) connected to the stainless-steel electrodes of the PFC device. The results were collected after a short equilibration period of ± 1 minute after exposure to sunlight.

3. Results and Discussion

3.1. Photoanode Performance vs. Soot Oxidation Capacity

The photocatalytic soot oxidation and photoanode performance in the gas phase of five different pure single-phase photocatalysts (P25, PC500, $TiO_{2\ Qiu}$, $WO_{3\ Sigma}$, and $WO_{3\ Mart.}$) were studied in our previous works [21,30].

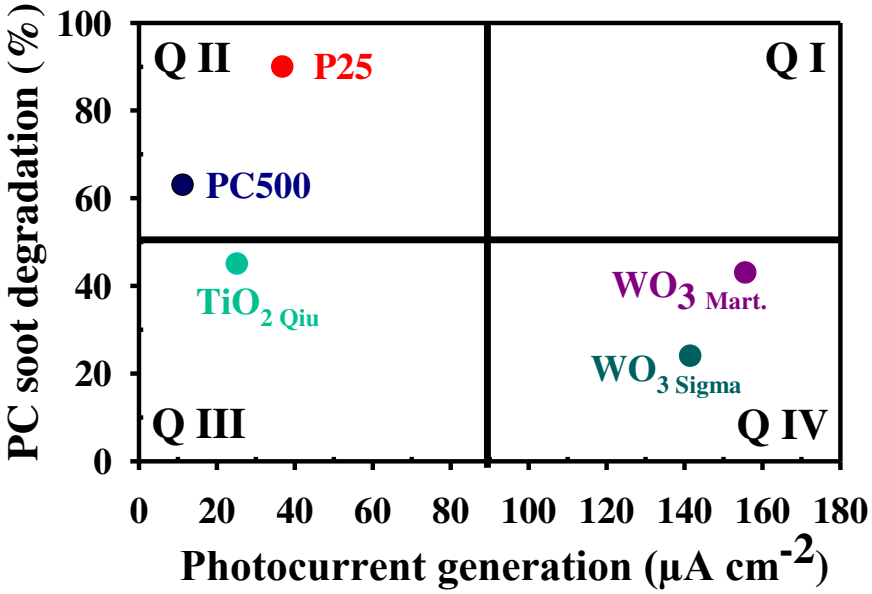

Figure 2. Comparison of the photocatalytic soot degradation after 11 days under UV light (2.1 mW cm^{-2}) to the instant photocurrent generation from CA measurements under AM 1.5G simulated solar light (100 mW cm^{-2}) when flushing the PFC device with a moist methanol vapour (17 mmol m^{-3}). Extracted with permission from our previous works [21,30], Q = Quadrant.

Figure 2 gives an overview of photoanode performance and the soot oxidation capability of each TiO_2 and WO_3-based photocatalyst. No photocatalysts are present in the preferred quadrant I, evidencing that in general, TiO_2-based photocatalysts are better soot degraders, but poor photoanodes (quadrant II and the top of quadrant III), whereas WO_3-based photocatalysts perform better as photoanodes in a gas phase PFC device but are less efficient soot degraders (quadrant IV). Therefore, in this study, the best performing TiO_2 and WO_3-based photocatalysts are combined to couple the beneficial properties of both pure photocatalysts, thus aiming to synthesise a photocatalyst that lies in quadrant I. Among the three studied TiO_2-based photocatalysts, P25 is the most efficient soot degrader. As a result, P25 was the TiO_2- based photocatalyst selected for further study. A slightly better performance was seen in the all-gas phase PFC while using $WO_{3\ Mart.}$ as a photoanode, thus selecting $WO_{3\ Mart.}$ as the WO_3-based photocatalyst for further experiments. In this study, the first aim is to evaluate the performance of P25, $WO_{3\ Mart.}$ and their different combinations for separate and combined soot oxidation and VOC degradation in the PFC device. The second aim is to replicate the operation of a PFC device using sunlight in a highly soot-containing environment. Since the ability of the photoanode to degrade the soot

without fouling the active catalytic sites will be crucial to achieve a robust and long-term operation of the device in a highly polluted environment.

3.2. Material Characterisation

The physicochemical properties of both selected pure photocatalysts (P25 and $WO_{3\ Mart.}$) have been studied extensively in the literature or by the manufacturer [35,36]. **Table 1** shows an overview of relevant properties from different techniques, including UV-VIS spectroscopy, BET (Brunauer-Emmett-Teller) surface area analysis, and X-ray diffraction, for both pure and combined photocatalysts. A more detailed explanation on these physico-chemical characterization results is given in the supplementary information (XRD (**Figure S5**), BET analysis (**Figure S6-7**) and UV-Vis Spectroscopy (**Figure S8-9**)).

Table 1. Physical characteristics of commercial/synthesised materials (band gap, BET surface area and crystallite particle size).

Material	Band gap Eg (eV)[4]	Surface area BET ($m^2\ g^{-1}$)	Crystallite particle size (nm)[5,6]
$P_{25\ Evonik}$[1]	3.12	52	19 (A), 32 (R)
$WO_{3\ Mart.}$[2]	2.6	9	32 (W)
P_{25}-$WO_{3\ Mart,\ mass}$[3]	2.6/3.12	31	19 (A), 32 (R), 32 (W)
P_{25}-$WO_{3\ Mart,\ mol}$[3]	2.6/3.12	24	19 (A), 32 (R), 32 (W)

1) *Commercially available photocatalyst*
2) *Synthesized based on the literature protocols*
3) *Photocatalyst synthesized by mixing two pure photocatalysts*
4) *Obtained by the Tauc method applied on diffuse reflectance spectra*
5) *Estimated values from XRD using the Debye-Scherrer equation*
6) *Material crystal phase A= Anatase, R=Rutile, W= Monoclinic Polymorph*

Scanning electron microscopy micrographs are used to study the morphology of materials and thin films under consideration. **Figure 3(a)** represents the cross-sectional view of P25 on $WO_{3\ Mart.}$ (0.4/1.6) on a glass slide used for photocatalytic soot oxidation measurements. P25 and $WO_{3\ Mart.}$ have been divided into separate layers, with P25 at the top and $WO_{3\ Mart.}$ at the bottom, also confirmed using energy-dispersive X-ray spectroscopy (EDX) maps. The difference in density between TiO_2 and $WO_{3\ Mart.}$ results in a different layer thickness ratio (~5.5 µm TiO_2 and ~7.2 µm $WO_{3\ Mart.}$) from that of the 0.4/1.6 wt.% ratio used to identify the samples. A top view of the film and an EDX map are also presented. A similar pattern has also been observed in other samples with $WO_{3\ Mart.}$ on P25, wherein the $WO_{3\ Mart.}$ is on top and P25 is at the bottom. **Figure 3(b)** represents the top view of P25 on $WO_{3\ Mart.}$ on a carbon

paper used for PFC experiments. We can observe using EDX maps that P25 is deposited in patches on $WO_{3\ Mart.}$ in the network of carbon paper. A cross-sectional view is not obtained due to the low loading and complexity of the carbon paper network.

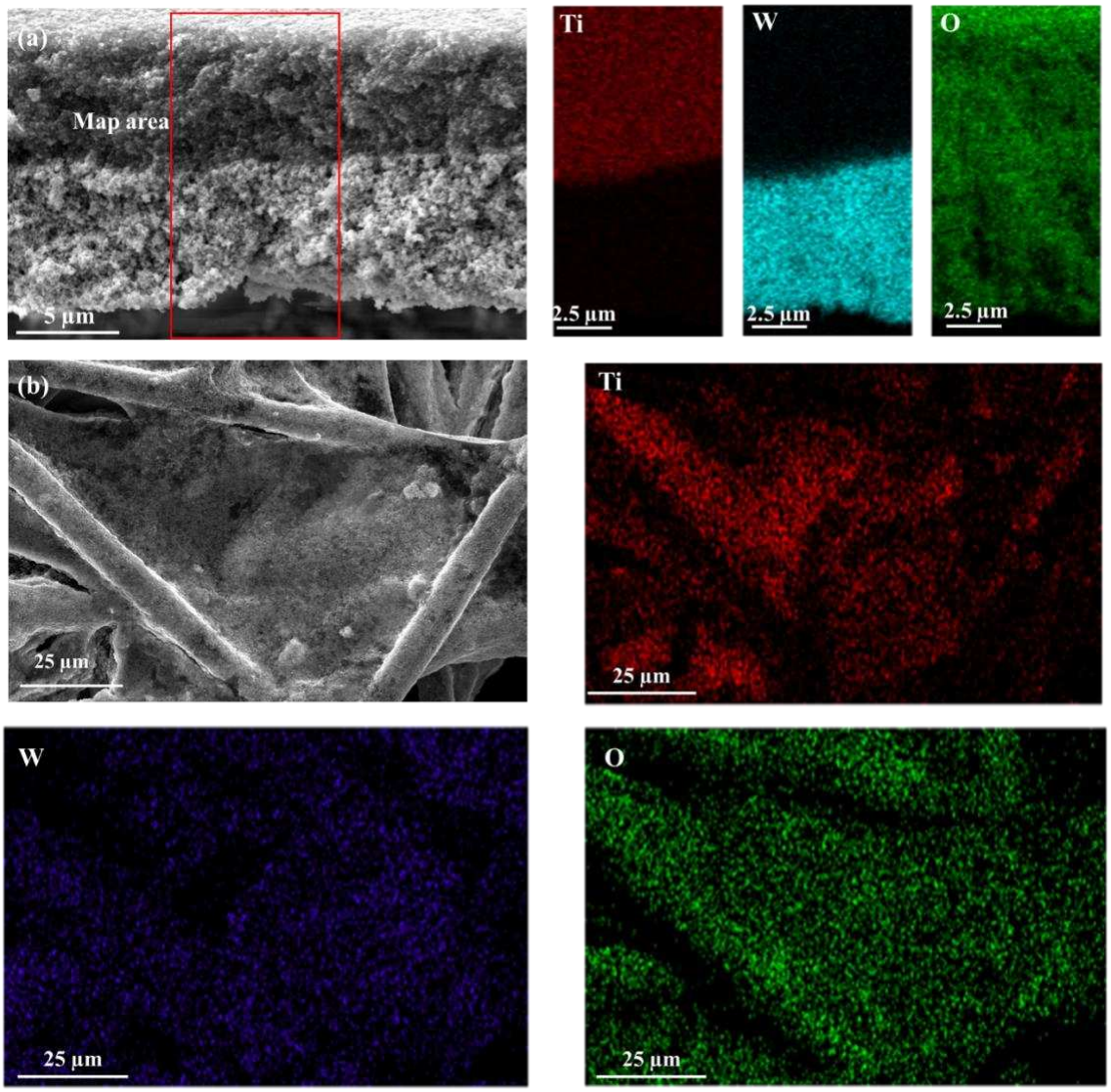

Figure 3. Scanning Electron Microscopy images of the best-performing combination (a) cross-sectional view of P25 on $WO_{3\ Mart.}$ (0.4/1.6) on glass slide along with EDX map of Ti, W and O, (b) Top view of P25 on $WO_{3\ Mart.}$ (0.4/1.6) on carbon paper along with an EDX map of Ti, W and O.

3.3. Photo fuel cell experiments

The performance of the combined TiO_2-WO_3 photocatalysts as photoanode in the homemade PFC device was studied under simulated solar light (AM 1.5G, UV and Visible), with water vapour and moist methanol vapour with a concentration of 17 mmol m^{-3}. In **Figure 4**, the activity of P25 on $WO_{3\ Mart.}$ (0.4/1.6) in both the water and methanol vapour phase, which is the best-performing layered

combination among all others in the methanol vapour phase and it also outperformed the best layered combination in the water vapour phase (P25 on $WO_{3\ Mart.}$ (1.6/1.6). The activity of the best performing mixed combination using P25 and $WO_{3\ Mart.,\ mol}$ is given in **Figure S14** of the supplementary information.

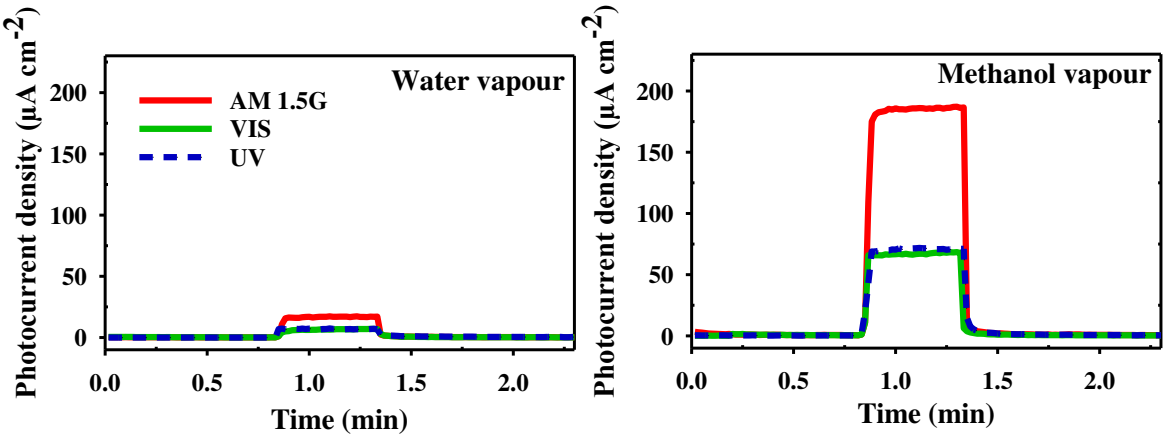

Figure 4. Photocurrent density as a function of time when using different light sources (simulated solar light (AM 1.5G, 100 mW cm^{-2}), visible light (> 420 nm, 96 mW cm^{-2}) and UV light (4 mW cm^{-2})), both when feeding the photoanode with pure water vapour **(a)** and moist methanol vapour **(b)** (17 mmol m^{-3}) using P25-$WO_{3\ Mart.}$ (0.4/1.6) as photoanode.

The results of all other studied combinations are summarised in **Figure 5**. When flushed with methanol vapour, the photocurrent generated with the best-performing combination (P25 on $WO_{3\ Mart.}$ (0.4/1.6)) is twice as high as that obtained with the best-performing mixed combination (P25-$WO_{3\ Mart.,\ mol}$). Upon the addition of methanol vapour in the photoanode feed, a clear increase in the photocurrent is observed in all tested photocatalysts which is mainly due to the hole-scavenging capability of methanol, which forms unstable H_3CO^* radicals as an intermediate while oxidizing, and sequentially, inject an electron into the conduction band of the photocatalyst[40,41]. Thus, one absorbed photon can generate both photogenerated and injected electrons (radical-generated electrons), resulting in current doubling. the effect is even more pronounced under applied electric bias, with significantly reduced recombination of generated charge carriers [1]. Additional chronoamperometric analysis of pristine and best-performing combinations using methanol vapour as feed is given in Figure S20 of the supporting information to validate the reproducibility of the measurements, as well as the long-term stability of the prepared photoanodes.

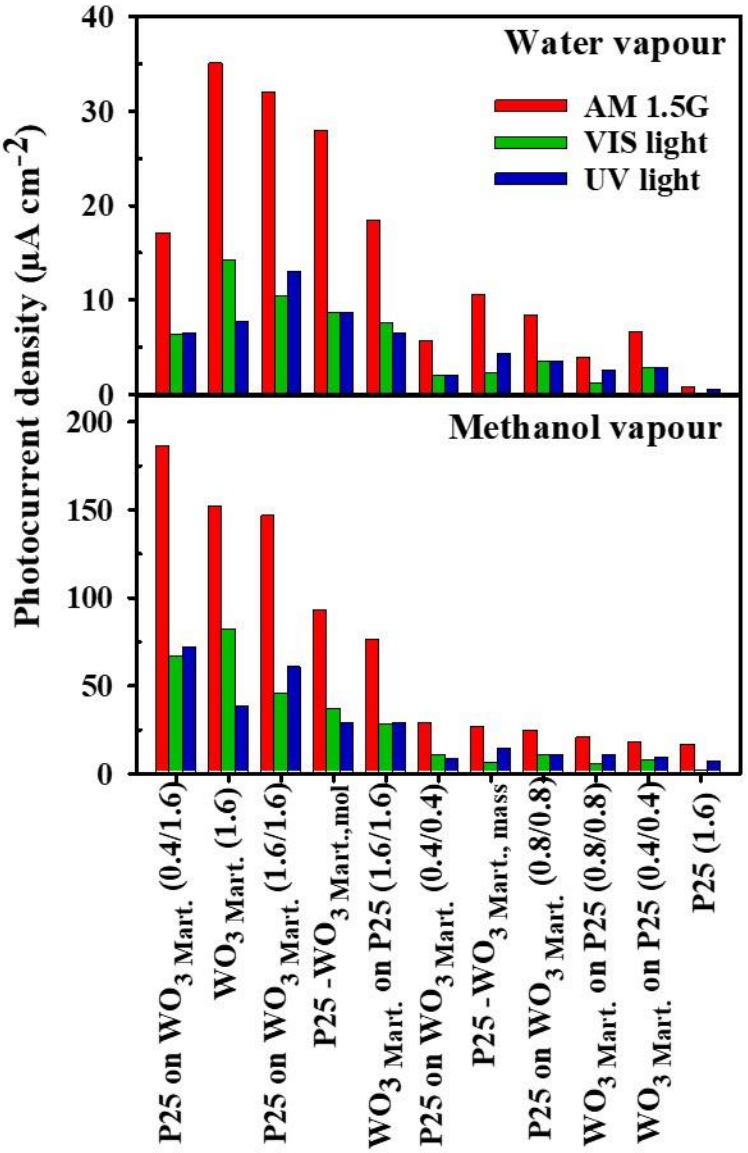

340

341 **Figure 5.** Photocurrent densities generated by different TiO_2-WO_3 combinations using different
342 illumination sources, both when flushing the PFC with (top) water vapour and (bottom) moist methanol
343 vapour with a concentration of 17 mmol m^{-3}.

344 From **Figure 5**, it is further clear that under simulated solar light, the combinations with a layer of
345 P25 on top of $WO_{3\ Mart.}$ performed better than those with a layer of $WO_{3\ Mart.}$ on top of P25. We attribute
346 this to the beneficial migration of charge carriers that reduce the recombination in P25 on top of WO_{3}
347 $_{Mart.}$, and the occurrence of photochromism in case of higher $WO_{3\ Mart.}$ content, which reduces the activity
348 for the samples with $WO_{3\ Mart.}$ on top of P25. This can be further explained by the transmittance data in
349 **Figure 6**, which demonstrate a larger fraction of solar and VIS light is available after passing a layer of
350 P25 compared to $WO_{3\ Mart.}$ Similar results were observed under simulated solar light with methanol

vapour in the feed for equal amounts of P25 and $WO_{3\ Mart.}$ (1.6/1.6) and pure $WO_{3\ Mart.}$. The higher photocurrent generation under VIS light for pure $WO_{3\ Mart.}$ is almost completely outweighed by the increase in photocurrent generation under UV light when adding a layer of P25 on top. Also, significant photocurrent generation is obtained with P25 on $WO_{3\ Mart.}$ (1.6/1.6) under VIS light. Reducing the amount of P25 in the combination (P25 on $WO_{3\ Mart.}$ (0.4/1.6) results in higher photocurrent generation when flushing with methanol. This increase is attributed to the increased transmittance of light through the top, thinner P25 layer, resulting in higher light utilization by the visible light active $WO_{3\ Mart.}$ bottom layer. When compared to standard $WO_{3\ Mart.}$ (1.6 mg cm^{-2}), the photocurrent generation increased by 87% and 22% under UV and simulated solar light, respectively, with the addition of a thin P25 layer (0.4 mg cm^{-2}) on top of $WO_{3\ Mart.}$ The solar light response lies between that of pure P25 and $WO_{3\ Mart.}$, resulting in a 2.6 times higher photocurrent generation under simulated solar light compared to UV light.

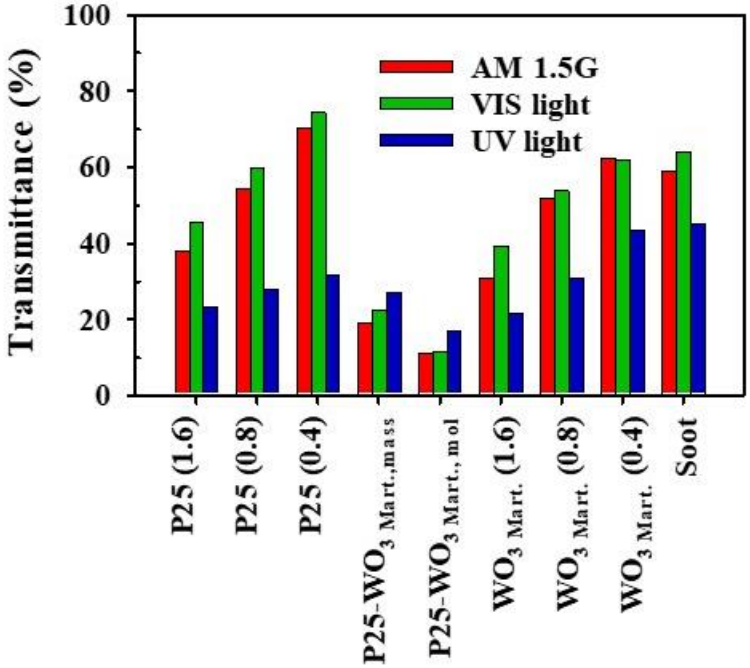

Figure 6. Transmittance (%) of simulated solar light (AM 1.5G, 100 mW cm^{-2}), visible light (> 420 nm, 96 mW cm^{-2}) and UV-A light (4 mW cm^{-2}) through a glass slide coated with a photocatalyst or a soot layer (22 µg cm^{-2}). The photocatalyst loading is shown between brackets (in mg cm^{-2}). The lamp was positioned 4 cm from the spectroradiometer, the glass slide was placed in the middle.

The best performing mixed TiO_2-WO_3 combination, P25-$WO_{3\ Mart.,\ mol}$, generates 5.2 times more photocurrent than pure P25 under solar light and when flushed with methanol vapour, while achieving 62% of the photocurrent generated by pure $WO_{3\ Mart.}$. When simply mixing both photocatalysts on a

mass basis, intermediate results were obtained. When lowering the amount of $WO_{3\ Mart.}$, as is the case for P25-$WO_{3\ Mart.,\ mass}$ (*ca.* 1/4 mol% WO_3 *vs.* 1/2 mol% WO_3 for P25-$WO_{3\ Mart.,\ mol}$), lower photocurrents were generated.

3.4. Photocatalytic Soot Oxidation

The photocatalytic soot oxidation capabilities of prepared combinations and pristine photocatalysts were studied using a digital image analysis method[20,21]. The method allows to discriminate between a homogeneously spread soot haze, and concentrated soot spots present on the samples. The difference between uniform soot haze, concentrated spots and comparison between day 0 to day 82 is shown in **Figure S10** in the supporting information. **Figure 7** shows the percentage soot degradation capacity of all prepared combinations in terms of soot haze and spots for different time intervals (0-60 days).

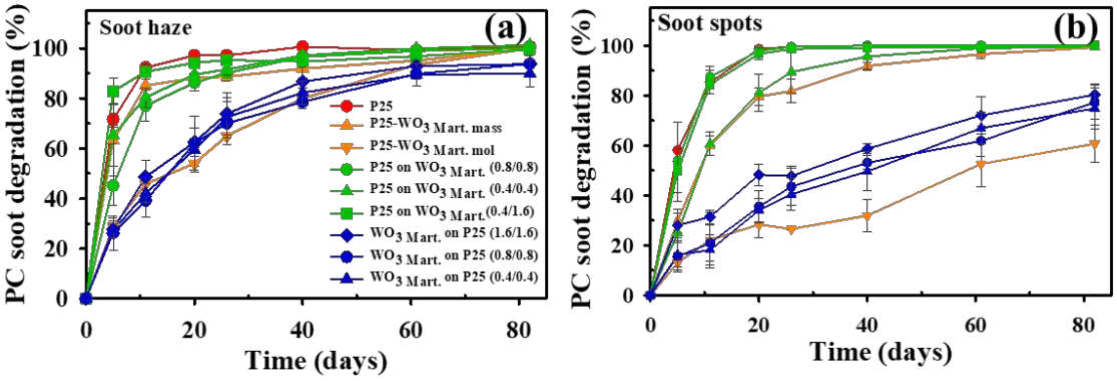

Figure 7. Photocatalytic soot degradation of the **(a)** soot haze and **(b)** concentrated soot spots by a range of photocatalysts determined by digital image analysis after light-induced colour-change correction, as a function of UV illumination time. The error bars are based on three independent samples. Lines are added to guide the reader's eye

Figure 7 (a) shows the soot degradation activity by monitoring the disappearance of the uniform soot haze. P25 is the fastest soot degrader, reaching complete oxidation after 40 days, and is closely followed by all other combinations with P25 on top of $WO_{3\ Mart.}$, all of which reached > 95% degradation after 40 days. P25-$WO_{3\ Mart.}$ reached 92%, $WO_{3\ Mart.}$ on P25 (1.6/1.6) reached 87%, and all other combinations reached around 80 % degradation of soot haze after 40 days. It can be concluded that in a layered configuration, the top layer plays a pivotal role in the soot oxidation capacity. As a result, combinations with P25 on the top of $WO_{3\ Mart.}$ showed a similar soot degradation capability to pure P25 due to its facile charge transport and suitable band position for the degradation [18,20]. In accordance,

393 the soot haze degradation rates of layered combinations with $WO_{3\ Mart.}$ on top of P25 are also remarkably
394 similar, but relatively lower than the combinations with P25 on top. These results agree well with results
395 obtained previously with pure $WO_{3\ Mart.}$ [20].

396 While depositing soot on top of the photocatalyst layer, only a negligible amount of particles will
397 penetrate the active photocatalyst layer. The activity initially increases with the film thickness due to
398 the generation of more excited charge carriers, but saturates after the active layer becomes thicker than
399 the maximum diffusion length of the charge carriers [42]. Even when decreasing the photocatalyst
400 loading four times, the top layer remains sufficiently thick (~5 µm) to rule out the effect of the bottom
401 layer. Indeed, the diffusion length of photogenerated charge carriers is only in the order of nanometres
402 [42,43]. When mixing the photocatalysts, the combinations with a higher ratio of P25 content to $WO_{3\ Mart.}$
403 showed better activity towards soot degradation, as expected since P25 is a more active soot degrader
404 under UV illumination.

405 In view of concentrated soot spot degradation, all the combinations with P25 on top of $WO_{3\ Mart.}$
406 were the best-performing samples and coincided with the results of pure P25. The layered combinations
407 with $WO_{3\ Mart.}$ on top of P25 exhibited significantly lower degradation rates than the combinations with
408 P25 as the top layer. No separate soot experiments were performed under artificial sunlight or visible
409 light only, due to the very time-intensive nature of these measurements, and the dominating contribution
410 of UV-driven photoactivity once titania species are involved in the matrix.

411 *3.5. Photoanode performance vs. Soot oxidation capability*

412 The performance of each (composite) photocatalyst was separately tested towards
413 photocatalytic soot degradation and as a photoanode in the gas phase PFC with 17 mmol m^{-3} of methanol
414 or water vapour. To attain an efficient and soot-resistant waste gas-to-electricity PFC device outdoors,
415 it is vital to have good performance towards both reactions. The results are visually summarised in
416 **Figure 8**.

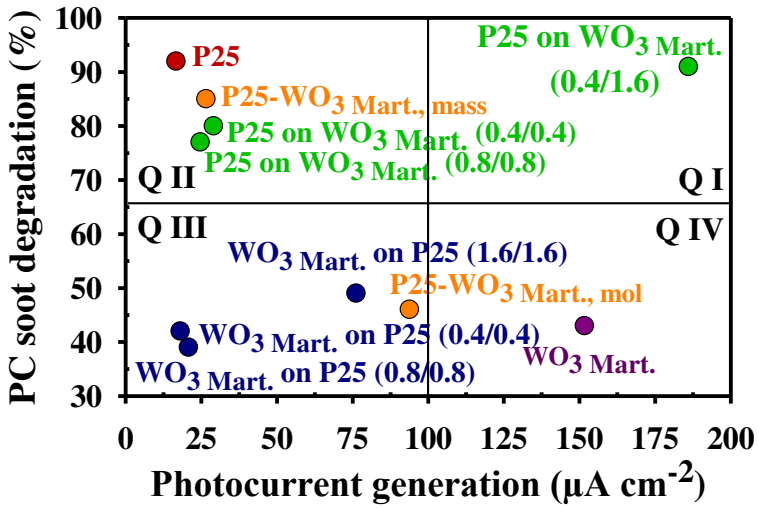

Figure 8. Comparison of studied photocatalysts, plotting the photocatalytic soot degradation after 11 days under UV light (2.1 mW cm^{-2}) against the photocurrent generation (extracted from CA measurements) under simulated solar light (100 mW cm^{-2}), when flushing the PFC device with moist methanol vapour (17 mmol m^{-3}). The following photocatalysts are studied: (red) pure P25, (purple) pure $WO_{3\ Mart.}$, (green) layered P25 on $WO_{3\ Mart.}$ combinations, (blue) layered $WO_{3\ Mart.}$ on P25 combinations, and (orange) mixed P25-$WO_{3\ Mart.}$ combinations. Q = quadrant.

In **Figure 8**, P25 on $WO_{3\ Mart.}$ (0.4/1.6) with a four times less dense P25 layer on top of a standard $WO_{3\ Mart.}$ layer with 1.6 mg cm^{-2} outperformed all other studied photocatalysts both in terms of soot oxidation and photoanode performance. It is the only photocatalyst that lies in quadrant I, achieving the targeted combination of excellent photoanode performance with efficient photocatalytic soot degradation. The other photocatalyst combinations with P25 on top, or with higher loading (*i.e.,* pure P25, or P25-$WO_{3\ Mart.,\ mass}$) lie in quadrant II and show better activity towards photocatalytic soot oxidation but act poorly as photoanodes. On the other hand, photocatalysts containing higher loadings of $WO_{3\ Mart.}$ (*i.e.,* pure $WO_{3\ Mart.}$, and P25-$WO_{3\ Mart.,\ mol}$), or $WO_{3\ Mart.}$ on top of P25, all show less efficient photocatalytic soot degradation and lie in quadrants III and IV. The combinations with the less dense top layer of $WO_{3\ Mart}$ performed worse as photoanodes and are in the left corner of quadrant III. The P25 on $WO_{3\ Mart.}$ (0.4/1.6) sample thus combines the high soot oxidation capacity of P25 with the excellent photoanode properties of the underlying $WO_{3\ Mart.}$ layer. This configuration results in a 23% higher PFC performance than pure $WO_{3\ Mart.}$ while maintaining a photocatalytic soot oxidation capacity that is almost

as good as for pure P25. These results indicate the suitability of this photoanode for application in a direct sunlight-driven gas phase PFC device operating in highly soot-contaminated environments.

3.6. Combined PFC and Soot Oxidation

The operation of gas-phase PFC devices in soot-contaminated environments, especially in urban and industrial areas, will result in the continuous deposition of soot on the electrode surface. With time, the thickness of the soot layer will increase, which eventually blocks the active electrode surface and also shields it from incoming light, thus reducing the overall performance of the PFC device. In this section, the effect of soot thickness, degradation time, and oxidation capability was studied using the best-performing catalyst combination consisting of P25 on $WO_{3\ Mart.}$ (0.4/1.6) during the PFC operation in the presence and absence of hole scavengers. The digital image analysis method was applied to quantify the degradation of soot on the photoanode during PFC operation. Pure P25 and $WO_{3\ Mart.}$ were also studied as a benchmark.

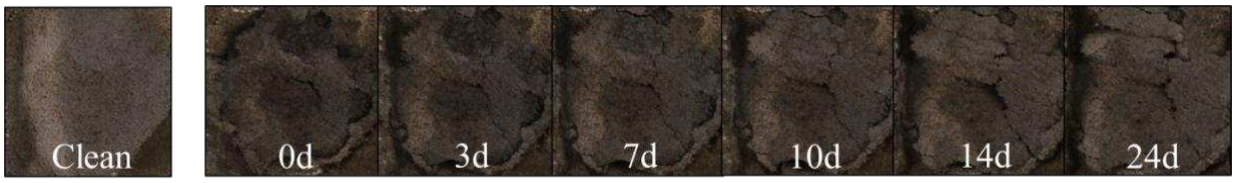

Figure 9. Subsequent digital images of soot degradation on a PFC photoanode coated with P25 when flushed with water vapour. A photoanode without soot (clean), with soot before UV illumination (0d) and after 3, 7, 10, 14 and 24 days of UV illumination. The initial dark background originates from the use of conductive carbon paper for the photoelectrocatalyst deposition and MEA fabrication.

In **Figure 9**, the degradation of soot during PFC operation is visible as the brightening of the photoanode surface with time. This brightening is reflected in the shift of most frequent L* values to higher L* values (brighter) against the number of pixels in **Figure 10(a)**. The digital image analysis method developed by Van Hal *et al*. [20,21] to quantitatively monitor the photocatalytic soot degradation, was also applied here to quantify the soot degradation rate during PFC operation. Colour correction was not required as the photoanode compartment of the PFC device was constantly flushed with either water vapour or moist methanol vapour, preventing dehydration that might cause discolouration of the photoanode surface. The soot degradation results obtained by the three studied photocatalysts are shown in **Figure 10(b).**

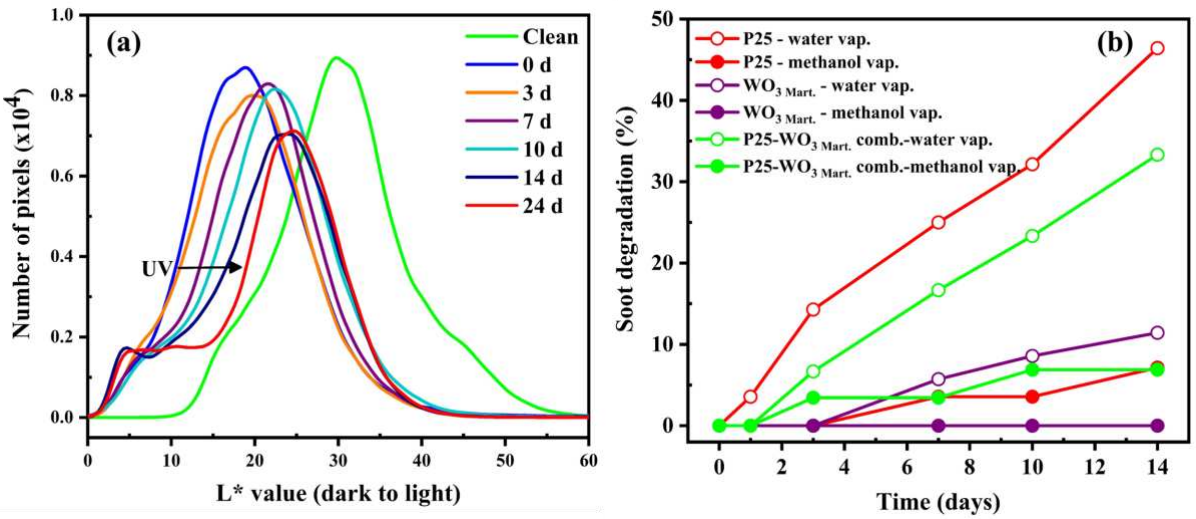

Figure 10. (a) Number of pixels plotted against the L* value, representing the degradation of soot on a P25 photoanode during PFC operation when using water vapour as a photoanode feed. **(b)** Soot degradation, determined by digital image analysis, as a function of UV illumination time. P25 on $WO_{3\ Mart.}$ (0.4/1.6) is denoted as 'P-W comb'.

When comparing the combined soot degradation with PFC **(Figure 10b)** to the obtained results from the direct photocatalytic soot degradation of different combinations **(Figure 8),** it is quite notable that pure P25 was able to degrade over 90% of the uniform soot haze after 11 days in direct photocatalytic experiments (ambient air, relative humidity (RH) ~ 33%), while only 32% of soot haze was degraded after 10 days during the combined PFC operation under moist air with relative humidity (RH) of ~65%. A similar trend was also observed for the other two photocatalysts: 43% *vs.* 9% degradation for $WO_{3\ Mart}$ and 91% *vs.* 23% for P25 on $WO_{3\ Mart.}$ (0.4/1.6). The experimental conditions in the combined and direct experiments unavoidably differ in many ways, including the substrate, setup and relative humidity, which complicates a direct absolute comparison. Mainly, the lower RH in the direct photocatalytic soot degradation is more favourable for soot oxidation over water oxidation, thus enhancing the soot degradation rate. On the other hand, qualitatively, the order in soot oxidation capability follows the same trend as expected from the isolated photocatalytic soot degradation experiments: P25 > P25 on $WO_{3\ Mart.}$ (0.4/1.6) > WO_3.

The obtained results from the soot degradation by digital image analysis followed a clear linear trend, *i.e.,* zero-order kinetics, up until 14 days under UV illumination, as shown in **Figure 10(b)**. The

485 calculated soot degradation rate during the PFC operation of the three studied photoanodes is given in
486 **Table 2**.

487 **Table 2**. The soot degradation rate of studied photoanodes in PFC flushed with water vapour or
488 methanol vapour (17 mmol m^{-3}) under UV illumination.

	Soot degradation rate (µg cm^{-2} day^{-1})	
	In water vapour	**In methanol vapour**
P25	0.75 ± 0.02	0.10 ± 0.01
P25 on $WO_{3\ Mart.}$ (0.4/1.6)	0.52 ± 0.01	0.12 ± 0.01
$WO_{3\ Mart.}$	0.18 ± 0.01	0 ± 0

489

490 For all three studied photocatalysts, the soot degradation rate obtained when flushing the
491 photoanode compartment with water vapour is much higher than the rate obtained when flushing with
492 methanol vapour. Since methanol is a well-known efficient hole scavenger, [44,45] this result suggests
493 that soot is, at least in part, being photo-oxidized by direct interaction with the photogenerated holes.
494 Thus, the presence of methanol in the photoanode feed increases the competition for the oxidizing
495 species and decreases the degradation rate of soot under UV illumination. As a result, the current
496 doubles, as evidenced by CA measurements with and without methanol vapour in the photoanode feed.
497 When using moist methanol vapours as photoanode feed, no soot degradation was obtained by pure
498 $WO_{3\ Mart.}$ after 14 days. The addition of a four times less dense P25 layer (0.4 mg cm^{-2}) on top of a
499 standard $WO_{3\ Mart.}$ layer (1.6 mg cm^{-2}) increased the soot oxidation capacity during PFC operation
500 substantially. This combined photocatalyst thus again performs well as a photoanode of an all-gas phase
501 PFC, exploiting the high electron mobility of the thick WO_3 layer for efficient PFC operation. A final
502 important advantage of this combined photocatalyst is the ability to use the visible light activity of WO_3
503 $_{Mart.}$, resulting in increased performance of the PFC device under sunlight. Furthermore, it is interesting
504 to note that the soot degradation rates obtained within the PFC device (**Table 2**), even in the presence
505 of methanol, convincingly evidence the potential practical applicability of this technology for tackling
506 urban soot depositions, which typically vary between 0.001 - 0.010 µg cm^{-2} per day [46–48]. The tested
507 material combination can remove soot deposits at least ten times faster.

508

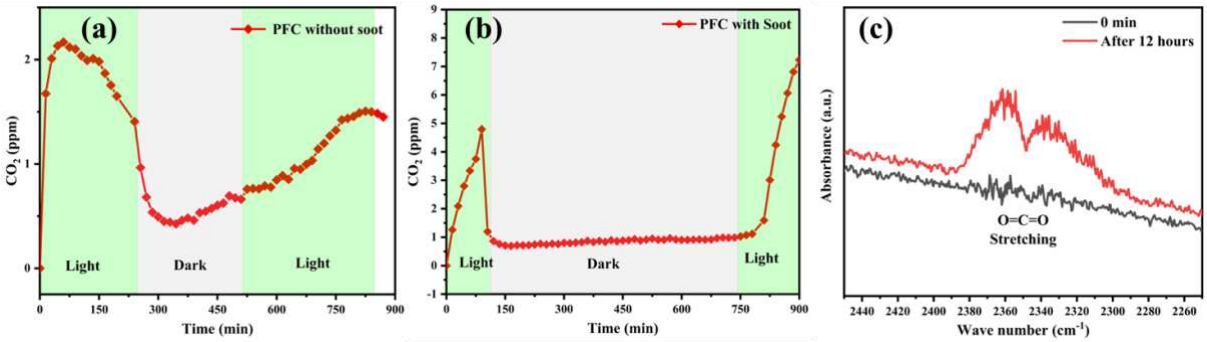

Figure 11. The measured concentration of carbon dioxide (CO_2) during the long-term operation of PFC using P25-$WO_{3\ Mart.}$ (0.4/1.6) **(a)** PFC without soot. **(b)** PFC with soot. **(c)** *In situ* FTIR spectra collected for P25-$WO_{3\ Mart.}$ (0.4/1.6) before and after 12 h during the photocatalytic soot degradation experiment.

The mechanistic pathway for both soot degradation on the one hand, and the mechanism of the PFC on the other hand, were studied in previous works [49,50]. To ensure catalytic stability and analyse the formed products using GC, we conducted long-term PFC experiments on the best-performing combination of P25-WO_3. The GC measurements (**Figure 11 a and b**) clearly demonstrate that the presence of soot increases the CO_2 level from 2 ppm to 5-7 ppm under illumination, providing further evidence of the simultaneous abatement of VOC and soot during PFC operation.

To gain a better understanding of the surface chemistry and intermediates formed during soot degradation, digital image analysis alone is insufficient as it only provides a visual representation of soot degradation at a specific time. Utilizing an airtight *in situ* FTIR cell while performing photocatalytic soot degradation provides a more detailed insight into formed intermediates and evolved products. This experiment has been performed for the best-performing P25-$WO_{3\ Mart.}$ composite. **Figure 11c** shows the FTIR signal corresponding to CO_2 evolution at 2290-2390 cm^{-1} (O=C=O, stretching) confirming the mineralization of soot to CO_2 after 12 h of UV illumination. Initially, the height of the CO_2 band increases rapidly and then flattens after 10 h due to the depletion of oxygen in the reaction chamber. The complete FTIR spectrum from 1000 to 3500 cm^{-1} is given in **Figure S19** of the supplementary information. Additionally, a very small band was observed in the region of 1273-1450 cm^{-1} corresponding to adsorbed formate species, hardly distinguishable from background noise. It is plausible that the other bands originating from these compounds are concealed due to steric hindrance. This is because the observed formate bound well to the surface of the pellet [51]. Based on the *in situ* FTIR

results, we have confirmed the kinetic model proposed by Chin et al [49,52]. for photocatalytic soot oxidation, which assumes two pathways. Our observations support the theory of a single-step soot to CO_2 path, as evidenced by the formation of CO_2 before the increase of other bands. However, the intermediate species in the sequential path from soot to CO_2 is not a specific molecule, but rather a combination of intermediates involved in the oxidation process, as predicted by Chin et al[49,52]. Importantly, no trace of carbon monoxide (2150 cm^{-1}) was found with both *in situ* FTIR and GC measurements.

3.7. Charge Transfer Mechanism

To understand the charge transfer mechanism, the band edge position and Fermi level (conduction band minima) were calculated based on the combined results of UV-VIS DRS (**Figure S8,9**), Mott Schottky analysis (**Figure S15**) and theoretical band position calculations (**Figure S17**). The Mott Schottky plot of TiO_2 and $WO_{3\ Mart.}$ in **Figure S5**, confirms the n-type characteristics of both semiconductors, and the calculated Fermi levels of TiO_2 and $WO_{3\ Mart.}$ are -0.363 and 0.782 V vs NHE, respectively. The valence band (VB) and conduction band (CB) positions of TiO_2 and $WO_{3\ Mart.}$ were calculated by using Mulliken's electronegativity and the band gaps derived from the UV-VIS DRS spectra. The detailed band position calculation can be found in **Table S2**. The calculated valence and conduction band positions of pure TiO_2 are +2.767 and -0.352eV and those of $WO_{3\ Mart.}$ are +3.38 and +0.785 eV, respectively. Previous studies [53,54] and the calculated band positions, confirm a type II staggered heterostructure formation between TiO_2 and $WO_{3\ Mart}$. The proposed energy band alignment of TiO_2/WO_3 heterostructures is schematically illustrated in **Figure 12 (right)**. Under irradiation, both TiO_2 and $WO_{3\ Mart.}$ are excited and produce photogenerated electrons and holes. The CB of $WO_{3\ Mart.}$ lies below the CB of TiO_2, thus the photogenerated electrons move from the CB of TiO_2 to the CB of $WO_{3\ Mart.}$. Photogenerated holes, on the other hand, migrate in the opposite direction, from VB of WO_3 to VB of TiO_2. This opposite movement of photogenerated charge carriers (e^- and h^+) effectively increases the charge separation and reduces charge carrier recombination, [53] resulting in improved photocatalytic soot oxidation and photoanode performance. The photogenerated holes convert adsorbed water vapours on the catalytic surface of P25-$WO_{3\ Mart}$ into hydroxyl radicals •OH and H^+ cations. This occurs because

the valance band position of both TiO_2 and WO_3 is more positively located than the standard redox potentials of OH^-/H_2O (2.72 eV) and $H_2O/•OH$ (2.38 eV). Possibly WO_3 produces more •OH because of its higher valance band potential (3.382 eV) [53]. Thus, resulting in improved activity in the prepared composites.

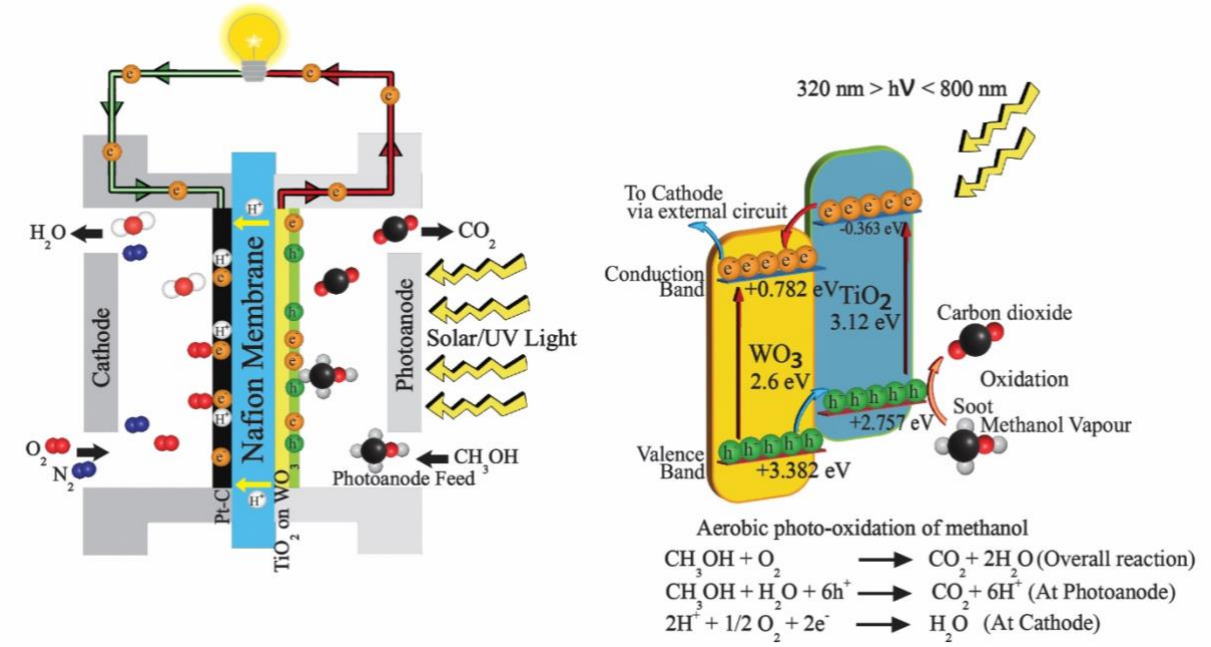

Figure 12. Schematic representation of photofuel cell working (left) and charge transfer mechanism of P25 WO_3 photoanode under illumination condition (right).

The best-performing layer combinations with TiO_2 on top of $WO_{3\ Mart.}$ and other mixed combinations follow the same trend in the band edge potential and charge transfer mechanism. Conversely, the heterostructures with WO_3 on top and higher loading of WO_3 exhibited low catalytic performance in both applications due to the accumulation of electrons in the conduction band of WO_3, which gives rise to the photochromic effect [55]. The occurrence of photochromism diminishes the catalytic activity due to the accumulated electrons reacting with OH* radicals to yield OH^- anions instead of reducing O_2 to superoxide radicals. This is facilitated by the fact that the potential for the OH^*/OH^- reaction takes precedence as it is situated at +1.9 eV while that of O_2/O_2^- is at -0.33 eV [53,56].

3.8. Outdoor Validation

The outdoor measurements were performed to study the real-life performance of our in-house developed PFC device and selected photoanodes for autonomous PFC operation. These measurements were performed at the University of Antwerp, Campus Groenenborger, Belgium, on a sunny day with an absolute sunlight irradiance of 57 mW cm^{-2} between 280 and 1100 nm (more precisely 2 mW/cm^{-2} between 280-400 nm and 35 mW cm^{-2} between 400 - 800 nm). **Figure 13(a)** shows the highest photocurrent density generated using $WO_{3\ Mart.}$ (26 µA cm^{-2}), closely followed by P25 on $WO_{3\ Mart.}$ (0.4/1.6) (23 µA cm^{-2}) and with exceptionally low photocurrent generated by P25 (2 µA cm^{-2}). The slightly better performance of $WO_{3\ Mart.}$ compared to P25 on $WO_{3\ Mart.}$ (0.4/1.6), is expected since soot deposits will not yet exert a manifest impact during this short-duration measurement. In time, however, it is expected that the P25 on $WO_{3\ Mart.}$ (0.4/1.6) will outperform $WO_{3\ Mart.}$ due to its superior soot degradation capability. **Figure 13(b)** shows the autonomously operating PFC device, solely driven by sunlight and outdoor air. The video of the real-time registration is provided as **Video S1** in the electronic supporting information.

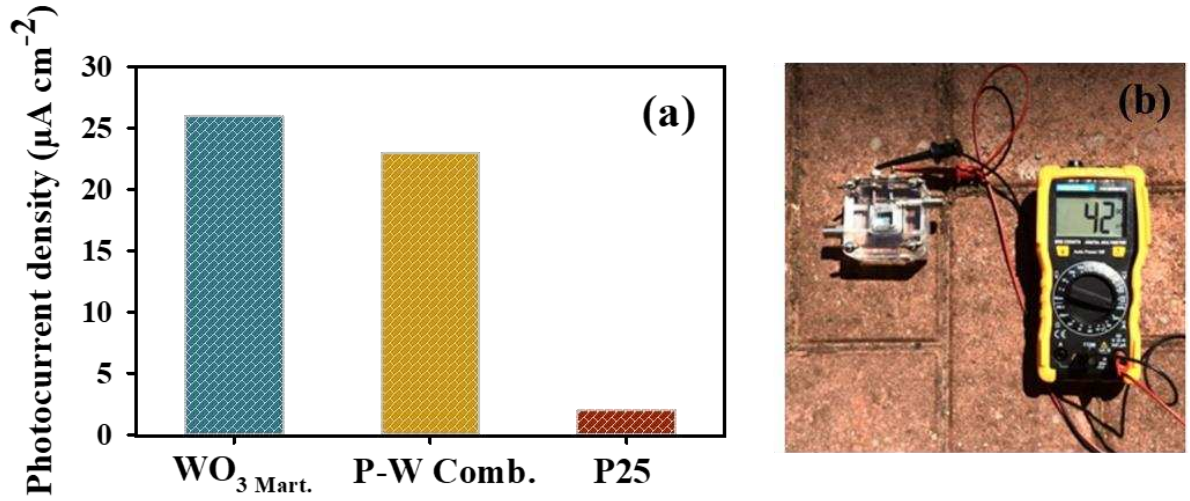

Figure 13. (a) Photocurrent density as a function of time when autonomously applying the PFC device outside (CGB, Antwerp), when using the following photocatalysts at the photoanode: $WO_{3\ Mart.}$, P25 on $WO_{3\ Mart.}$ (0.4/1.6) - denoted as 'P-W comb' - and P25. The measurement was performed on the 14th of June 2021 at 2 p.m., (b) Picture of outdoor application of PFC device, using P25 on $WO_{3\ Mart.}$ (0.4/1.6) as photoanode.

The best performing PFC configuration with $WO_{3\ Mart.}$ was also applied the same day in a more polluted area, *i.e.* on a bridge crossing the busiest highway in Belgium (Floraliënlaan over E19 highway, Ring of Antwerp), resulting in a significant 28% increase in the generated photocurrent. Cars and other

fossil fuel-based vehicles emit a broad range of pollutants, including VOCs, NO_x, and particulate matter (*e.g.,* soot) [13], resulting in an increased presence of hole scavengers, thereby increasing the photocurrent as in the test case with methanol. In contrast, most pollutants present in real outdoor air are more stable or complex, resulting in a lower instantaneous photocurrent increase compared to methanol. More research is required to get more insight into the effect of common waste gases/pollutants on PFC operation, eventually linking outdoor air sampling with on-site photocurrent measurements. The same applies for studying long-term stability effects and accumulation/degradation of soot deposits. However, this first proof of concept experiment already demonstrates the feasibility of the proposed technology in real life.

To mimic the PFC performance in low-light conditions, the experiment was repeated in a shaded area (**Video S2** in the supplementary information). From the results, it is quite evident that the cell retains over 70% of its activity under low-light conditions, which is encouraging for practical implementation. Overall, a critical note should be added that the produced photocurrents are still low in absolute terms, as only limited research has been performed on all-gas phase PFC devices and the current device is only of small lab-scale. We are confident, however, that progress in materials science and PEC cell engineering will effectively address this current shortcoming in the following years. Nonetheless, this study shows the first promising results striving towards an efficient and robust PFC device for real outdoor applications. We are hopeful that the described proof of concept can serve as a foundation for the further development of an autonomous, low-cost, and widely applicable gas-phase PFC system.

4. Conclusion

In this study, we have studied the application of an all-gas-phase PFC cell for simultaneous pollutant degradation and energy recovery. The main goal was to assess the compatibility of the PFC device with an environment that does not only contain gaseous pollutants, but also soot particles. It was found that a composite photoanode photoelectrocatalyst consisting of a four times less dense TiO_2 layer (0.4 mg cm^{-2}) on top of a $WO_{3\ Mart.}$ layer (1.6 mg cm^{-2}) resulted in a 22% increase in solar-driven photocurrent generation compared to pure $WO_{3\ Mart.}$ photoanodes when flushing the photofuel cell with methanol-rich vapours. Having (less dense) TiO_2 (P25) in the top layer proved to be critical to have

excellent photocatalytic soot degradation capabilities, while having $WO_{3\ Mart.}$ in the bottom layer was crucial to have performant photocurrent generation. While a significant decrease in the soot degradation rate was measured in combined simultaneous soot degradation and PFC operation experiments in the presence of methanol vapours, the resulting soot degradation rate of (0.12 ± 0.01) µg cm^{-2} day^{-1} is still at least ten times faster than typical soot deposition rates in an urban environment, while at the same time, the generated photocurrent remains largely unaffected. Finally, our in-house engineered PFC device was applied outside, evidencing autonomous PFC operation solely using actual sunlight and real outdoor air. Overall, the four times less dense TiO_2 (P25) layer on top of a $WO_{3\ Mart.}$ layer showed promising results towards an efficient, sunlight-driven, and soot-resistant waste gas-to-electricity PFC device. The particular configuration of a thin layer of an efficient photocatalytic soot degrader on top of an excellent photoanode material, is the key to operate stable PFC in highly polluted areas, and offers a wide range of opportunities for future research.

CRediT authorship contribution statement

Karthick Raj AG: Conceptualization, Methodology, Electrochemical measurements, Formal analysis, Investigation, Data curation, Writing – original draft, Writing – review & editing, **Antony Charles Minja:** Electrochemical measurements, Formal analysis, Writing- review & editing, **Rajesh Reddy Ninakanti:** Microscopy analysis, Writing- review & editing, **Myrthe Van Hal:** Conceptualization, Methodology, Formal analysis, Data curation, Writing – original draft, **Fons Dingenen:** Writing- review & editing, **Rituraj Borah:** Writing- review & editing, **Sammy W. Verbruggen:** Conceptualization, Funding acquisition, Supervision, Writing- review & editing.

Acknowledgements

A.C.M. and S.W.V. kindly acknowledge the University of Antwerp Special Research Fund for a DOCPRO4 doctoral fellowship (FFB210298). M.V.H. and F.D. acknowledge the Research Foundation Flanders (FWO) for an aspirant doctoral fellowship (1135619N and 11F3722N, respectively).

Corresponding Author

Email: Sammy.Verbruggen@uantwerpen.be

ORCID

Karthick raj AG 0000-0003-2163-2413

Antony Charles Minja 0000-0003-1130-3325

Rajesh Reddy Ninakanti 0000-0002-7665-3548

Myrthe Van Hal 0000-0002-4717-6666

Fons Dingenen 0000-0002-7633-589X

Rituraj Borah 0000-0003-2424-0335

Sammy W. Verbruggen 0000-0003-2372-9630

Competing interests

The authors declare no competing financial interests.

Supporting Information

Supplementary information contains physiochemical (XRD, UV-Vis, SEM-EDAX and BET) and electrochemical (LSV, EIS, Mott Schottky plot and bode plot) characterizations of both pure P25 and $WO_{3\ Mart.}$ photosensitizers; Video of real-time outdoor application of photofuel cell using $WO_{3\ Mart.}$ and photocatalyst combination as photoanodes **(Video S1 and S2)**; Spectra of all used lamps and comparison of soot haze concentration spots.

References

[1] P. Lianos, Review of recent trends in photoelectrocatalytic conversion of solar energy to electricity and hydrogen, Appl Catal B. 210 (2017) 235–254. https://doi.org/10.1016/j.apcatb.2017.03.067.

[2] P. Lianos, Production of electricity and hydrogen by photocatalytic degradation of organic wastes in a photoelectrochemical cell. The concept of the Photofuelcell: A review of a re-emerging research field, J Hazard Mater. 185 (2011) 575–590. https://doi.org/10.1016/j.jhazmat.2010.10.083.

[3] F. Dingenen, S.W. Verbruggen, Tapping hydrogen fuel from the ocean: A review on photocatalytic, photoelectrochemical and electrolytic splitting of seawater, Renewable and Sustainable Energy Reviews. 142 (2021). https://doi.org/10.1016/j.rser.2021.110866.

[4] B.R. Stanmore, J.F. Brilhac, P. Gilot´laboratoire, G. Gilot´laboratoire, The oxidation of soot: a review of experiments, mechanisms and models, 2001.

[5] C. Andersen, Y. Omelekhina, B.B. Rasmussen, M. Nygaard Bennekov, S.N. Skov, M. Køcks, K. Wang, B. Strandberg, F. Mattsson, M. Bilde, M. Glasius, J. Pagels, A. Wierzbicka, Emissions of soot, PAHs, ultrafine particles, NOx, and other health relevant compounds from stressed burning of candles in indoor air, Indoor Air. 31 (2021) 2033–2048. https://doi.org/10.1111/ina.12909.

[6] M. Matti Maricq, Chemical characterization of particulate emissions from diesel engines: A review, J Aerosol Sci. 38 (2007) 1079–1118. https://doi.org/10.1016/j.jaerosci.2007.08.001.

[7] D. Massey, J. Masih, A. Kulshrestha, M. Habil, A. Taneja, Indoor/outdoor relationship of fine particles less than 2.5 μm (PM2.5) in residential homes locations in central Indian region, Build Environ. 44 (2009) 2037–2045. https://doi.org/10.1016/j.buildenv.2009.02.010.

[8] M. Stranger, S.S. Potgieter-Vermaak, R. Van Grieken, Characterization of indoor air quality in primary schools in Antwerp, Belgium, Indoor Air. 18 (2008) 454–463. https://doi.org/10.1111/j.1600-0668.2008.00545.x.

[9] M.M. Lunden, T.W. Kirchstetter, T.L. Thatcher, S. V. Hering, N.J. Brown, Factors affecting the indoor concentrations of carbonaceous aerosols of outdoor origin, Atmos Environ. 42 (2008) 5660–5671. https://doi.org/10.1016/j.atmosenv.2008.03.017.

[10] J. Wichmann, T. Lind, M.A.M. Nilsson, T. Bellander, $PM_{2.5}$, soot and NO2 indoor-outdoor relationships at homes, pre-schools and schools in Stockholm, Sweden, Atmos Environ. 44 (2010) 4536–4544. https://doi.org/10.1016/j.atmosenv.2010.08.023.

[11] R. Asahi, T. Morikawa, T. Ohwaki, K. Aoki, Y. Taga, Visible-Light Photocatalysis in Nitrogen-Doped Titanium Oxides, Science (1979). 293 (2001) 269–271. https://doi.org/10.1126/science.1061051.

[12] S.W. Verbruggen, TiO2 photocatalysis for the degradation of pollutants in gas phase: From morphological design to plasmonic enhancement, Journal of Photochemistry and Photobiology C: Photochemistry Reviews. 24 (2015) 64–82. https://doi.org/10.1016/j.jphotochemrev.2015.07.001.

[13] D. Chen, Y. Cheng, N. Zhou, P. Chen, Y. Wang, K. Li, S. Huo, P. Cheng, P. Peng, R. Zhang, L. Wang, H. Liu, Y. Liu, R. Ruan, Photocatalytic degradation of organic pollutants using TiO2-based photocatalysts: A review, J Clean Prod. 268 (2020). https://doi.org/10.1016/j.jclepro.2020.121725.

[14] Y. Kameya, K. Torii, S. Hirai, M. Kaviany, Photocatalytic soot oxidation on TiO_2 microstructured substrate, Chemical Engineering Journal. 327 (2017) 831–837. https://doi.org/10.1016/j.cej.2017.06.094.

[15] A. Mills, J. Wang, M. Crow, Photocatalytic oxidation of soot by P25 TiO_2 films, Chemosphere. 64 (2006) 1032–1035. https://doi.org/10.1016/j.chemosphere.2006.01.077.

[16] S.K. Lee, S. McIntyre, A. Mills, Visible illustration of the direct, lateral and remote photocatalytic destruction of soot by titania, J Photochem Photobiol A Chem. 162 (2004) 203–206. https://doi.org/10.1016/j.nainr.2003.07.002.

[17] M.C. Lee, W. Choi, Solid phase photocatalytic reaction on the Soot/TiO2 interface: The role of migrating OH radicals, Journal of Physical Chemistry B. 106 (2002) 11818–11822. https://doi.org/10.1021/jp026617f.

[18] M. Smits, Y. Ling, S. Lenaerts, S. Van Doorslaer, Photocatalytic removal of soot: Unravelling of the reaction mechanism by EPR and in situ FTIR spectroscopy, ChemPhysChem. 13 (2012) 4251–4257. https://doi.org/10.1002/cphc.201200674.

[19] M. Smits, C. kit Chan, T. Tytgat, B. Craeye, N. Costarramone, S. Lacombe, S. Lenaerts, Photocatalytic degradation of soot deposition: Self-cleaning effect on titanium dioxide coated cementitious materials, Chemical Engineering Journal. 222 (2013) 411–418. https://doi.org/10.1016/j.cej.2013.02.089.

[20] M. Van Hal, S. Lenaerts, S.W. Verbruggen, Photocatalytic soot degradation under UV and visible light, Environmental Science and Pollution Research. (2022). https://doi.org/10.1007/s11356-022-23804-0.

[21] M. Van Hal, S.W. Verbruggen, X.-Y. Yang, S. Lenaerts, T. Tytgat, Image analysis and in situ FTIR as complementary detection tools for photocatalytic soot oxidation, Chemical Engineering Journal. 367 (2019) 269–277. https://doi.org/10.1016/j.cej.2019.02.154.

[22] X. Chen, J. Ye, S. Ouyang, T. Kako, Z. Li, Z. Zou, Enhanced Incident Photon-to-Electron Conversion Efficiency of Tungsten Trioxide Photoanodes Based on 3D-Photonic Crystal Design, ACS Nano. 5 (2011) 4310–4318. https://doi.org/10.1021/nn200100v.

[23] H. Wang, T. Lindgren, J. He, A. Hagfeldt, S.E. Lindquist, Photolelectrochemistry of nanostructured WO_3 thin film electrodes for water oxidation: Mechanism of electron transport, Journal of Physical Chemistry B. 104 (2000) 5686–5696. https://doi.org/10.1021/jp0002751.

[24] C. Santato, M. Ulmann, J. Augustynski, Enhanced Visible Light Conversion Efficiency Using Nanocrystalline WO_3 Films, Advanced Materials. 13 (2001) 511–514. https://doi.org/10.1002/1521-4095(200104)13:7<511::AID-ADMA511>3.0.CO;2-W.

[25] G. HODES, D. CAHEN, J. MANASSEN, Tungsten trioxide as a photoanode for a photoelectrochemical cell (PEC), Nature. 260 (1976) 312–313. https://doi.org/10.1038/260312a0.

[26] B. Seger, P. V. Kamat, Fuel cell geared in reverse: Photocatalytic hydrogen production using a TiO_2/Nafion/Pt membrane assembly with no applied bias, Journal of Physical Chemistry C. 113 (2009) 18946–18952. https://doi.org/10.1021/jp907367k.

[27] J. Georgieva, S. Armyanov, I. Poulios, S. Sotiropoulos, An all-solid photoelectrochemical cell for the photooxidation of organic vapours under ultraviolet and visible light illumination, Electrochem Commun. 11 (2009) 1643–1646. https://doi.org/10.1016/j.elecom.2009.06.019.

[28] J. Georgieva, TiO 2/WO 3 photoanodes with enhanced photocatalytic activity for air treatment in a polymer electrolyte cell, Journal of Solid State Electrochemistry. 16 (2012) 1111–1119. https://doi.org/10.1007/s10008-011-1504-7.

[29] J. Georgieva, S. Armyanov, I. Poulios, A.D. Jannakoudakis, S. Sotiropoulos, Gas phase photoelectrochemistry in a polymer electrolyte cell with a titanium dioxide/carbon/nafion photoanode, Electrochemical and Solid-State Letters. 13 (2010). https://doi.org/10.1149/1.3465306.

[30] M. Van Hal, R. Campos, S. Lenaerts, K. De Wael, S.W. Verbruggen, Gas phase photofuel cell consisting of WO_3- and TiO_2-photoanodes and an air-exposed cathode for simultaneous air purification and electricity generation, Appl Catal B. 292 (2021) 120204. https://doi.org/10.1016/j.apcatb.2021.120204.

[31] M.V. Dozzi, S. Marzorati, M. Longhi, M. Coduri, L. Artiglia, E. Selli, Photocatalytic activity of TiO_2-WO_3 mixed oxides in relation to electron transfer efficiency, Appl Catal B. 186 (2016) 157–165. https://doi.org/10.1016/j.apcatb.2016.01.004.

[32] M. Dahl, Y. Liu, Y. Yin, Composite Titanium Dioxide Nanomaterials, Chem Rev. 114 (2014) 9853–9889. https://doi.org/10.1021/cr400634p.

[33] L.F. Paula, M. Hofer, V.P.B. Lacerda, D.W. Bahnemann, A.O.T. Patrocinio, Unraveling the photocatalytic properties of TiO_2/WO_3 mixed oxides, Photochemical and Photobiological Sciences. 18 (2019) 2469–2483. https://doi.org/10.1039/c9pp00163h.

[34] B. Ohtani, O.O. Prieto-Mahaney, D. Li, R. Abe, What is Degussa (Evonic) P25? Crystalline composition analysis, reconstruction from isolated pure particles and photocatalytic activity test, J Photochem Photobiol A Chem. 216 (2010) 179–182. https://doi.org/10.1016/j.jphotochem.2010.07.024.

[35] Technical Data Sheet- Aeroxide P25 Evonik, (n.d.). https://www.productcenter.coating-additives.com/pdf/daten/engl/AEROXIDE_TiO2_P_25.pdf (accessed December 5, 2022).

[36] A. Martínez-de la Cruz, D.S. Martínez, E.L. Cuéllar, Synthesis and characterization of WO_3 nanoparticles prepared by the precipitation method: Evaluation of photocatalytic activity under vis-irradiation, Solid State Sci. 12 (2010) 88–94. https://doi.org/10.1016/j.solidstatesciences.2009.10.010.

[37] T. Tytgat, B. Hauchecorne, M. Smits, S.W. Verbruggen, S. Lenaerts, Concept and Validation of a Fully Automated Photocatalytic Test Setup, SLAS Technol. 17 (2012) 134–143. https://doi.org/10.1177/2211068211424554.

[38] K. Gelderman, L. Lee, S.W. Donne, Flat-Band Potential of a Semiconductor: Using the Mott–Schottky Equation, J Chem Educ. 84 (2007) 685. https://doi.org/10.1021/ed084p685.

[39] B. Hauchecorne, T. Tytgat, D. Terrens, F. Vanpachtenbeke, S. Lenaerts, Validation of a newly developed FTIR in situ reactor: Real time study of photocatalytic degradation of nitric oxide, Infrared Phys Technol. 53 (2010) 469–473. https://doi.org/10.1016/j.infrared.2010.09.008.

[40] E. Kalamaras, P. Lianos, Current Doubling effect revisited: Current multiplication in a PhotoFuelCell, Journal of Electroanalytical Chemistry. 751 (2015) 37–42. https://doi.org/10.1016/j.jelechem.2015.05.029.

[41] R. Memming, Semiconductor Electrochemistry, Wiley, 2015. https://books.google.be/books?id=9OhdBgAAQBAJ.

[42] T. Luttrell, S. Halpegamage, J. Tao, A. Kramer, E. Sutter, M. Batzill, Why is anatase a better photocatalyst than rutile? - Model studies on epitaxial TiO2 films, Sci Rep. 4 (2015). https://doi.org/10.1038/srep04043.

[43] P. Lianos, Environmental Review of recent trends in photoelectrocatalytic conversion of solar energy to electricity and hydrogen, Appl Catal B. 210 (2017) 235–254. https://doi.org/10.1016/j.apcatb.2017.03.067.

[44] Y. Tamaki, A. Furube, M. Murai, K. Hara, R. Katoh, M. Tachiya, Direct Observation of Reactive Trapped Holes in TiO_2 Undergoing Photocatalytic Oxidation of Adsorbed Alcohols: Evaluation of the Reaction Rates and Yields, J Am Chem Soc. 128 (2006) 416–417. https://doi.org/10.1021/ja055866p.

[45] T.M. El-Morsi, W.R. Budakowski, A.S. Abd-El-Aziz, K.J. Friesen, Photocatalytic Degradation of 1,10-Dichlorodecane in Aqueous Suspensions of TiO_2 : A Reaction of Adsorbed Chlorinated

Alkane with Surface Hydroxyl Radicals, Environ Sci Technol. 34 (2000) 1018–1022. https://doi.org/10.1021/es9907360.

[46] M. Smits, D. Huygh, B. Craeye, S. Lenaerts, Effect of process parameters on the photocatalytic soot degradation on self-cleaning cementitious materials, Catal Today. 230 (2014) 250–255. https://doi.org/10.1016/j.cattod.2013.10.001.

[47] M. Ferm, J. Watt, S. O'Hanlon, F. de Santis, C. Varotsos, Deposition measurement of particulate matter in connection with corrosion studies, Anal Bioanal Chem. 384 (2006) 1320–1330. https://doi.org/10.1007/s00216-005-0293-1.

[48] A. Chabas, T. Lombardo, H. Cachier, M.H. Pertuisot, K. Oikonomou, R. Falcone, M. Verità, F. Geotti-Bianchini, Behaviour of self-cleaning glass in urban atmosphere, Build Environ. 43 (2008) 2124–2131. https://doi.org/10.1016/j.buildenv.2007.12.008.

[49] P. Chin, G.W. Roberts, D.F. Ollis, Kinetic modeling of photocatalyzed soot oxidation on titanium dioxide thin films, Ind Eng Chem Res. 46 (2007) 7598–7604. https://doi.org/10.1021/ie070083t.

[50] S.W. Verbruggen, M. Van Hal, T. Bosserez, J. Rongé, B. Hauchecorne, J.A. Martens, S. Lenaerts, Harvesting Hydrogen Gas from Air Pollutants with an Unbiased Gas Phase Photoelectrochemical Cell, ChemSusChem. 10 (2017) 1413–1418. https://doi.org/10.1002/cssc.201601806.

[51] M. Smits, Y. Ling, S. Lenaerts, S. Van Doorslaer, Photocatalytic removal of soot: Unravelling of the reaction mechanism by EPR and in situ FTIR spectroscopy, ChemPhysChem. 13 (2012) 4251–4257. https://doi.org/10.1002/cphc.201200674.

[52] P. Chin, C.S. Grant, D.F. Ollis, Quantitative photocatalyzed soot oxidation on titanium dioxide, Appl Catal B. 87 (2009) 220–229. https://doi.org/10.1016/j.apcatb.2008.09.020.

[53] N. Moghni, H. Boutoumi, H. Khalaf, N. Makaoui, G. Colón, Enhanced photocatalytic activity of TiO_2/WO_3 nanocomposite from sonochemical-microwave assisted synthesis for the photodegradation of ciprofloxacin and oxytetracycline antibiotics under UV and sunlight, J Photochem Photobiol A Chem. 428 (2022). https://doi.org/10.1016/j.jphotochem.2022.113848.

[54] X. Sun, W. He, T. Yang, H. Ji, W. Liu, J. Lei, Y. Liu, Z. Cai, Ternary TiO_2/WO_3/CQDs nanocomposites for enhanced photocatalytic mineralization of aqueous cephalexin: Degradation mechanism and toxicity evaluation, Chemical Engineering Journal. 412 (2021) 128679. https://doi.org/10.1016/j.cej.2021.128679.

[55] A.O.T. Patrocinio, L.F. Paula, R.M. Paniago, J. Freitag, D.W. Bahnemann, Layer-by-Layer TiO_2/WO_3 Thin films as efficient photocatalytic self-cleaning surfaces, ACS Appl Mater Interfaces. 6 (2014) 16859–16866. https://doi.org/10.1021/am504269a.

[56] J. Yang, X. Zhang, H. Liu, C. Wang, S. Liu, P. Sun, L. Wang, Y. Liu, Heterostructured TiO_2/WO_3 porous microspheres: Preparation, characterization and photocatalytic properties, Catal Today. 201 (2013) 195–202. https://doi.org/10.1016/j.cattod.2012.03.008.

848 **Graphical abstract**

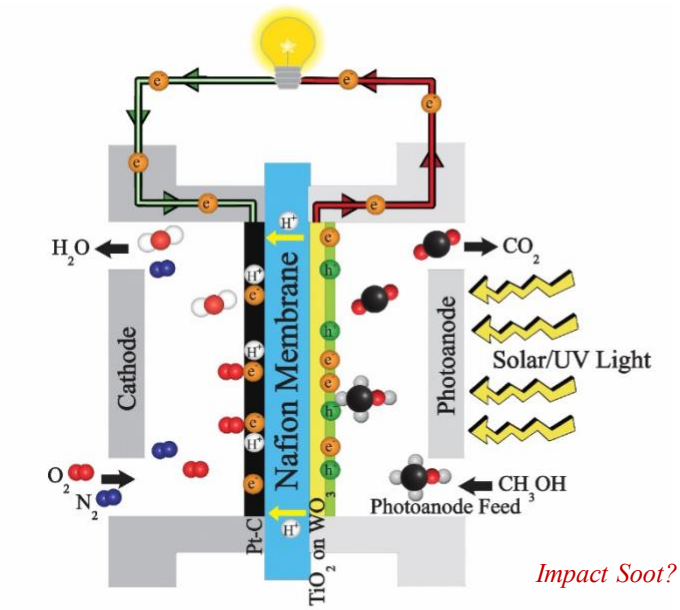

849